2012 IEEE International Conference on Robotics and Automation
RiverCentre, Saint Paul, Minnesota, USA
May 14-18, 2012

Wind field estimation for autonomous dynamic soaring

Jack W. Langelaan
Aerospace Engineering, Penn State University
email: jlangelaan@psu.edu

John Spletzer, Corey Montella
Computer Science and Engineering
Lehigh University

Joachim Grenestedt
Mechanical Engineering
Lehigh University

***Abstract*— A method for distributed parameter estimation of a previously unknown wind field is described. The application is dynamic soaring for small unmanned air vehicles, which severely constrains available computing while simultaneously requiring updates that are fast compared with a typical dynamic soaring cycle. A polynomial parameterization of the wind field is used, allowing implementation of a linear Kalman filter for parameter estimation. Results of Monte Carlo simulations show the effectiveness of the approach. In addition, in-flight measurements of wind speeds are compared with data obtained from video tracking of balloon launches to assess the accuracy of wind field estimates obtained using commercial autopilot modules.**

I. INTRODUCTION

Dynamic soaring of birds was first described by Lord Rayleigh in 1883 [1] and discussed in more detail in 1889 [2]. While it seems to be a much more recent idea, the potential for dynamic soaring of aircraft has actually been recognized since at least 1909 [3], and dynamic soaring of full sized aircraft has been studied at several times over the past century [4], [5], [6]. With the advent of low cost electronics and the first demonstrations of radio-control dynamic soaring, the potential for long duration flight by unmanned aerial vehicles (UAVs) has recently become an area of research [7]. The possibility of dynamic soaring in the shear layer near the jet stream is discussed by Sachs and da Costa [8].

An overview of the instrumentation required for full scale dynamic soaring is discussed by Kiceniuk [9]. Detailed results of dynamic soaring flight tests conducted at the Dryden Flight Research Center are described by Gordon [10].

Typically dynamic soaring is cast as a trajectory optimization problem with an *a priori* known wind field [11]. Unfortunately this will not be available during flight; moreover, to the authors' knowledge there are currently no sensors that can be carried on a small UAV that can measure the 3D wind field ahead of the vehicle. A means of mapping or predicting the wind field using only on-board measurements is therefore required. There are two components to wind mapping: first, estimating wind velocity given measurements aboard the vehicle; second, incorporating these estimates in a three-dimensional map of the mean wind field.

Since the purpose of the wind map is to enable real-time trajectory planning it must satisfy several requirements, including: (a) it must be updated in real time; (b) the trajectory planner must be able to query the map very quickly; and (c) uncertainty in the map must be computed to enable robust trajectory planning.

In [12] Lawrance and Sukkarieh describe a method for wind field estimation based on Gaussian Process Regression. Their approach has the benefit of being applicable to arbitrary wind fields, but suffers from slow updates, making real-time implementation problematic. In contrast to that work, here we seek to develop a method for wind field estimation that uses known structure to simplify estimation.

During dynamic soaring, the cyclic trajectory implies that the volume of air "inhabited" by the vehicle is limited in size, with dimensions dependent on the trajectory parameters. For soaring in the near-ground shear layer the vertical dimension is of order 10–100m with similar scales for the cross-wind and downwind dimensions. The preliminary results described above for jet stream dynamic soaring show that a volume approximately 1 km $\times$ 1 km $\times$ 1 km is required. In addition, dynamic soaring (especially that employed by albatrosses and human RC glider pilots) typically exploits wind fields with fairly simple structure. This wind field consists of a mean spatially varying component with temporally varying terms (i.e. gusts) superimposed. Generally the vertical gradient is significantly stronger than horizontal gradients, and the rate of change of the mean wind field is fairly slow compared with the time required to fly a single cycle. Combined with the relatively limited volume occupied during dynamic soaring, this structure can be exploited to simplify the mapping problem, making it tractable for real-time implementation. The estimation problem is thus cast as a parameter estimation problem, where a smooth function is used to model the wind field and the parameters of this function are estimated using measurements obtained at discrete, distributed points.

Since in-flight wind field estimation relies on *in situ* measurements of wind speed, we also briefly discuss wind velocity measurements. Results of in-flight measurements are compared with measurements of wind velocity collected using vision-based tracking of balloons. While time- and space-synchronization of balloon and aircraft data is problematic, we show that the aircraft can obtain reasonable measurements of wind velocity in-flight.

The remainder of this paper describes wind field estimation (Section II), presents results of Monte Carlo simulations (Section III), describes results of a hardware experiment (Section IV) and presents concluding remarks (Section V).

978-1-4673-1405-3/12/$31.00 ©2012 IEEE

II. WIND FIELD ESTIMATION

The problem at hand is to estimate a continuous, smooth function that captures the spatial variation of the mean wind field. The mean wind field is assumed to vary slowly with time: here slowly means that several DS cycles can be flown before significant change in mean wind speed occurs.

Note that direct measurements of wind velocity are not available. Rather, these must be computed in-flight based on data measured by an autopilot module onboard the aircraft. The wind field is then estimated using the computed wind velocities.

A. Wind velocity computation

A method for computing wind velocity and an associated uncertainty analysis using sensors typically available in an autopilot module (e.g. GPS position and velocity, air speed, rate gyros, accelerometers) is given in [13]. For convenience results are summarized here.

Components of the wind field can be computed from ground-relative velocity (available from GPS) and air speed:

$$\begin{aligned} w_{ix} &= \dot{x} - v_a \cos\gamma \cos\beta \cos\psi \\ &\quad + v_a \cos\gamma \sin\beta \sin\psi \qquad (1) \\ w_{iy} &= \dot{y} - v_a \cos\gamma \cos\beta \sin\psi \\ &\quad - v_a \cos\gamma \sin\beta \cos\psi \qquad (2) \\ w_{iz} &= \dot{z} - v_a \sin\gamma \qquad (3) \end{aligned}$$

Here $w_{ix},\ w_{iy},\ w_{iz}$ are xyz components of the wind vector expressed in the inertial frame, $\dot{x},\ \dot{y},\ \dot{z}$ are components of aircraft velocity with respect to the inertial frame (obtained from GPS), v_a is airspeed, γ is flight path angle with respect to the air, β is sideslip angle, and ψ is heading. It is assumed that the autopilot module provides estimates of angles.

For zero-mean Gaussian measurement noise the uncertainty in computed wind field can be computed by linearizing the above equations about the current flight condition so that

$$\mathbf{w} \approx g(\bar{\mathbf{z}}) + \mathbf{G}(\mathbf{z} - \bar{\mathbf{z}}) \qquad (4)$$

where $\mathbf{w} = [w_{ix}\ w_{iy}\ w_{iz}]^T$, $\mathbf{z} = [\dot{x}\ \dot{y}\ \dot{z}\ v_a\ \gamma\ \beta\ \psi]^T$ and $\mathbf{G} = \nabla g$, the Jacobian of the wind computation equations (Equation 1, 2, 3) with respect to the measurements $\mathbf{z}$. Then $\mathbf{\Sigma}_w = \mathbf{G}\mathbf{\Sigma}_z\mathbf{G}^T$, where $\mathbf{\Sigma}_z$ is the noise covariance associated with ground speed, orientation and air data measurements.

As described in [13], a measure of the uncertainty in horizontal magnitude is $R_w = \mathbf{\Sigma}_w(1,1) + \mathbf{\Sigma}_w(2,2)$:

$$\begin{aligned} R_w &= \sigma_{\dot{x}}^2 + \sigma_{\dot{y}}^2 + \sigma_{v_a}^2 \cos^2\gamma \\ &\quad + \sigma_\gamma^2 v_a^2 \sin^2\gamma + (\sigma_\beta^2 + \sigma_\psi^2) v_a^2 \cos^2\gamma \qquad (5) \end{aligned}$$

This immediately shows that a significant contributor to uncertainty in computed wind field is the vehicle's airspeed (through coupling with orientation uncertainty). The most accurate way to obtain in situ wind measurements is thus using a neutrally buoyant balloon!

Assuming that angles (flight path angle γ, heading ψ and sideslip β) can be obtained to an accuracy of 1°, at typical dynamic soaring speeds (ranging from 50 m/s to 150 m/s) the uncertainty in computed wind magnitude ranges from $\sigma = 1.26$ m/s to $\sigma = 3.71$ m/s.

B. Wind field estimation as distributed parameter estimation

1) Wind field parameterization: If DS is limited to only the boundary layer (so that only albatross-style DS is performed) then one can impose empirically-derived functions such as Prandtl's power law relationship [14]:

$$\frac{u}{U} \approx \left(\frac{h}{\delta}\right)^{1/7} \qquad (6)$$

where u is the wind speed, U is the free stream velocity, h is height above the surface and δ is the boundary layer thickness.

In this case a first order polynomial function in $\ln h$ can perfectly model the wind field. However, such specific parameterizations can lead to inaccurate representations if they are inappropriately applied. A more generically applicable parameterization is desirable: here a polynomial representation is used.

2) Polynomial representation of wind fields: For convenience the wind field is represented by three components: horizontal magnitude, horizontal direction, and vertical component. Each component is assumed to vary independently.

$$w(h) = \sum_{i=0}^{N} a_i \tilde{h}^{N-i} \qquad (7)$$

$$\phi_w(h) = \sum_{i=0}^{N} b_i \tilde{h}^{N-i} \qquad (8)$$

$$w_z(h) = \sum_{i=0}^{N} c_i \tilde{h}^{N-i} \qquad (9)$$

where $\tilde{h} = \frac{h-h_0}{\Delta h}$ is altitude shifted to a reference datum and non-dimensionalized by a scale factor. Dynamic soaring typically exploits spatial (especially vertical) gradient in magnitude, hence for compactness equations here will be developed only for vertical variation in magnitude.

The task of the estimator is thus to compute estimates $\hat{a}_i$ of the polynomial parameters defining the wind field. Clearly winds change with time as well as in space. The problem of wind parameter estimation is thus a dynamic estimation problem, and as formulated it is a linear parameter estimation problem, well suited to implementation as a Kalman filter.

C. Kalman Filter Design

Without an accurate model for the time rate of change of wind field, wind velocity is assumed to vary as a random walk, so that

$$\mathbf{a}_{k+1} = \mathbf{a}_k + \mathbf{n} \qquad (10)$$

where $\mathbf{a}$ is the vector of parameters defining the wind magnitude field and $\mathbf{n} = \mathcal{N}(0, \mathbf{Q})$.

Measurements of wind speed are taken as altitude varies with time, so that

$$w_k = \mathbf{H}_k \mathbf{a}_k + v \qquad (11)$$

where $\mathbf{H}_k = \left[\tilde{h}_k^N \;\; \tilde{h}_k^{N-1} \;\; \ldots 1\right]$ (from Equation 7).

Measurement noise v is assumed to be zero-mean and Gaussian, so that $v = \mathcal{N}(0, R_w + R_{gust})$. The two components reflect sensor dependent noise and the effect of measured gusts. Recall that we seek to estimate the mean wind field, and gusts are treated as noise superimposed on the mean wind field.

Note that R_w will vary with time: it is computed using Equation 5 and thus it depends on airspeed and flight path angle.

The Kalman filter equations for this distributed parameter estimation problem can now be summarized.

Prediction

$$\hat{\mathbf{a}}_{k|k-1} = \hat{\mathbf{a}}_{k-1|k-1} \tag{12}$$

$$\mathbf{P}_{k|k-1} = \mathbf{P}_{k-1|k-1} + \mathbf{Q} \tag{13}$$

Correction

$$\mathbf{P}_{k|k} = \left(\mathbf{P}_{k|k-1}^{-1} + \mathbf{H}_k^T (R_w + R_{gust})^{-1} \mathbf{H}_k\right)^{-1} \tag{14}$$

$$\mathbf{K}_k = \mathbf{P}_{k|k} \mathbf{H}_k^T (R_w + R_{gust})^{-1} \tag{15}$$

$$\hat{\mathbf{a}}_{k|k} = \hat{\mathbf{a}}_{k|k-1} + \mathbf{K}_k \left(w_k - \mathbf{H} a_{k|k-1}\right) \tag{16}$$

Note that this is a 1D measurement update, requiring only one (low order) matrix inverse to compute the covariance update. This can be performed very quickly even on low-power computation hardware.

D. Filter initialization

Under some conditions it may be possible to have an *a priori* estimate of the wind field (e.g. from satellite data). However, this will not always be the case and a means to initialize the Kalman filter must be provided. Here delayed initialization is performed: wind is measured at several altitudes, the Vandermonde matrix is generated using Equation 11 and a least squares solution of the wind field parameters is used to initialize the Kalman filter.

III. SIMULATION RESULTS

To assess the wind field parameter estimation Monte Carlo simulations of flight in a wind field typical of the shear layer near the jet stream were conducted. A DS cycle for a wind field defined by

$$w(h) = 0.01h - 100 \tag{17}$$

with h in meters and w in m/s was computed using the method described in [15] and the aircraft is assumed to follow this trajectory exactly. At a rate of 10Hz the aircraft uses autopilot data to compute wind speed and uncertainty in wind speed using Equation 1 through 3 and Equation 5. Sensor noise standard deviations are given in Table I. It is assumed that the wind field is gust-free.

The wind field estimator uses a first order polynomial to define the wind field (matching truth).

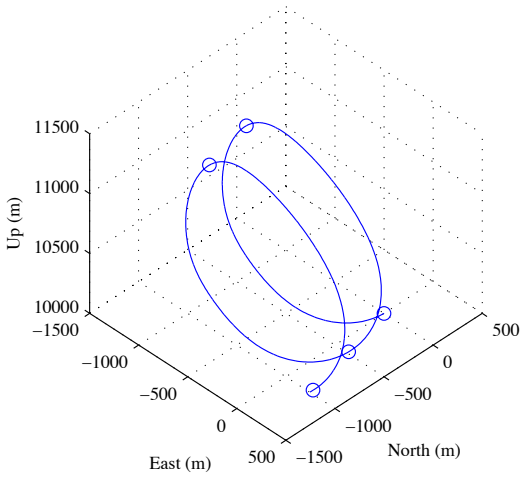

Fig. 1. Two loops of dynamic soaring cycle. Wind blows in the positive East direction, with magnitude increasing linearly with altitude.

TABLE I

SENSOR NOISE STANDARD DEVIATION FOR MONTE CARLO SIMULATIONS

parameter	**variable**	1σ **noise/uncertainty**
orientation	$\phi,\ \theta,\ \psi$	$\sigma_\phi = \sigma_\psi = 0,\ \sigma_\theta = 1^\circ$
air data	$v_a,\ \alpha,\ \beta$	$\sigma_v = 0.2$ m/s, $\sigma_\alpha = \sigma_\beta = 1^\circ$
ground speed	$\dot{x},\ \dot{y},\ \dot{z}$	0.1 m/s

Results of a representative run illustrate wind field estimation. Two loops of cyclic dynamic soaring are shown in Figure 1. A time history of the estimated wind field parameters is shown in Figure 2, with a_0 denoting the vertical gradient of the horizontal wind and a_1 denoting the wind speed at the datum (in this case $h_0 = 0$). The estimated parameters are well within estimated error bounds, with good convergence in parameters seen by about 0.4 loops. For dynamic soaring the key parameter is wind gradient, and this is well estimated.

Figure 3 shows the evolution of the estimated wind field during DS cycles, with plot times coinciding with the open symbols in Figure 1. The dotted red lines show the 2σ envelope of the uncertainty in estimated wind field. At time zero there is no estimate of the wind field. It is interesting to note the change in wind field uncertainty: at integer times (when the aircraft is at the bottom of a cycle) the wind field uncertainty is lowest at the bottom. At half-integer times (when the aircraft is at the top of the cycle) wind field uncertainty is reversed.

Results of Monte Carlo simulations show that the parameter estimation is consistent (i.e. the estimated error accurately predicts the actual error).

A measure of the accuracy of estimating the wind field is a mean error residual:

$$R = \frac{1}{N} \sum_{i=1}^{N} |w(h_i) - \hat{w}(h_i)| \tag{18}$$

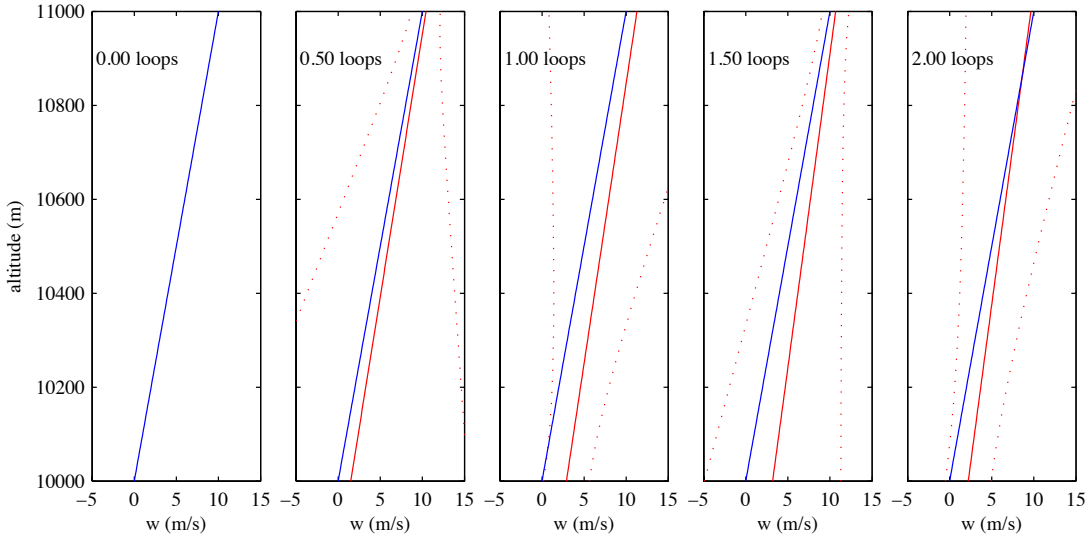

Fig. 3. Time history of wind field estimation for a representative run. Blue lines show the true wind velocity, solid red shows the estimated field and dotted red shows 2σ uncertainty bounds on the estimated wind field.

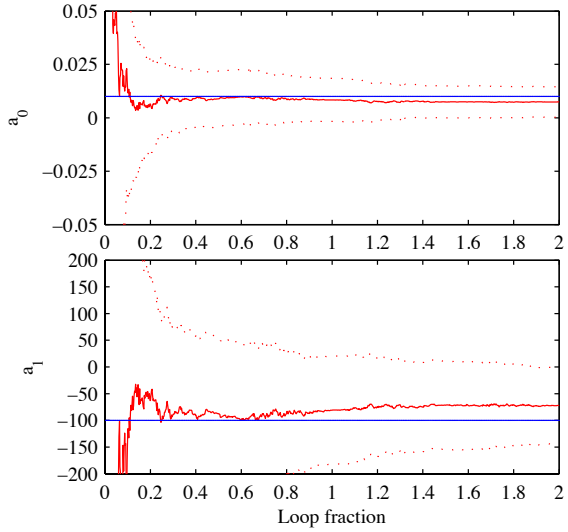

Fig. 2. Wind parameter estimation for a representative run. Blue lines show true parameter values, solid red shows the estimated parameter and dotted red shows 2σ bounds.

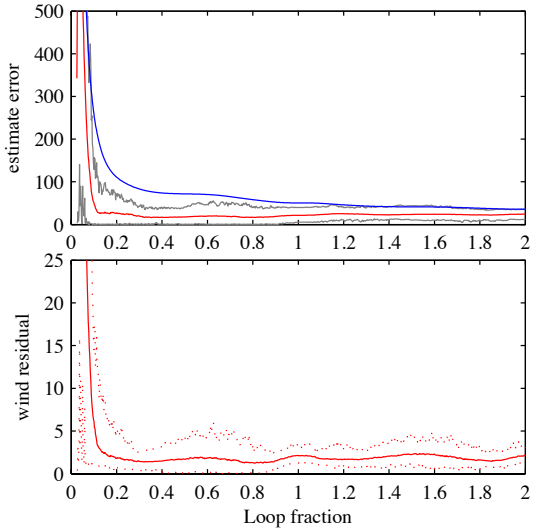

Fig. 4. Top: 2-norm of estimate error (mean: red; minimum/maximum: grey) and mean estimated error (blue). Bottom: Time history of residual error in estimated wind field.

where $h_i \in \{h_1\ h_2\ \ldots h_N\}$, a set of altitudes for evaluating actual and predicted wind. Figure 4(bottom) shows the mean residual (solid red) and the envelope of maximum/minimum residuals (dotted red) as DS cycles are flown. The mean error in wind magnitude for the estimated wind field is approximately 2 m/s, consistent with the error in the wind computation.

IV. EXPERIMENTAL RESULTS

A. Aircraft Platform

The aircraft development platform used in this work was designed and fabricated in-house at Lehigh University, and is shown at Figure 5. The planform is based upon an inverse Zimmerman design. It is made of two half ellipses, both having the same minor axis but the forward ellipse having a major axis that is three times that of the rear ellipse. A fixed fin was used in conjunction with two elevons. The design has very benign stall characteristics, is capable of operating safely in turbulent air, and can glide down steeply to land when required. Full stall landings at almost zero airspeed are easy with this aircraft.

This is clearly not a dynamic soaring aircraft, but it is suitable for collecting wind field data.

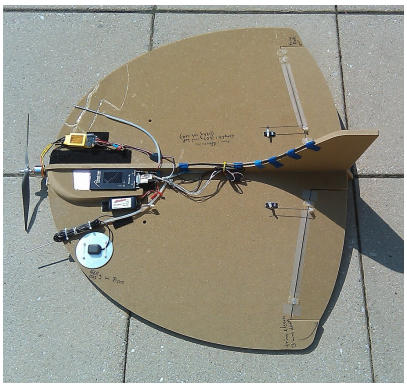

Fig. 5. Uglo 6 development platform used in this work. During testing, the aircraft was flown manually while telemetry data were logged via the on-board Piccolo SL autopilot system.

B. Ground Truth Wind Velocity Estimation

As stated previously, one of the primary objectives of this work was to demonstrate real-time wind mapping with an actual aircraft. In order to characterize the performance of the proposed approach, "ground truth" data were needed. While these were readily available for simulated wind fields, estimating wind velocities in proximity to an actual aircraft during flight was significantly more challenging. To address this requirement, we employed a vision-based approach for ground truth wind field estimation.

During flight testing, brightly colored balloons containing an air-helium mixture were released serially from the ground so their trajectories would carry them in the vicinity of the aircraft flight path. The balloons were then tracked over time using what amounted to a wide baseline (*e.g.*, 50-70 meter) stereo vision system using a pair of Point Grey Chameleon 1280x960 video camera systems that logged images at a rate of 2 Hz. Point correspondences between the two sets of camera images were then recovered manually for each balloon track during a post-processing phase. Using these correspondences in conjunction with a three-dimensional reconstruction approach based upon Hartley's method [16], the relative position and orientation of both camera systems, as well as the positions of the tracked balloons, were recovered to a scale factor. The scale factor was obtained by measuring the camera baseline. The balloon position estimates were then transformed to an earth-centered coordinate frame using GPS position estimates for the cameras, as well as measurements of camera azimuth and elevation from a compass and inclinometer, respectively. With the balloon positions known, their velocities – and as a consequence the Northing/Easting components of the wind field – were estimated using a finite difference approach vs. time with temporal smoothing to help mitigate high frequency noise.

To validate the the vision-based approach, initial experiments involved tracking a tethered balloon rig carrying an EagleTree eLogger V4 with a 10 Hz WAAS enabled GPS module as payload [17]. The motivation was to use the logged GPS velocities for benchmarking the vision system's tracking performance. A total of 6 launches were conducted from different initial positions at standoff distances of $\approx 110 - 180$ meters from the camera systems. The balloon rig was released at ground level, and allowed to rise with minimal resistance while attached to a 125 meter long, 0.15 mm diameter tether. Each trial was considered completed once the end of the tether was reached. Results from these experiments showed that the mean absolute deviation between the two velocity estimates vs. time for all trials was 0.35 m/s (minimum 0.22 m/s, maximum 0.55 m/s). Results from a single launch are shown at Figure 6 (right). Note that these error levels represent the compounding of *both* the vision tracker and GPS velocity errors. These results indicate that the vision-based tracking system provides an effective means for estimating the wind velocity at standoff distances in excess of 200 meters.

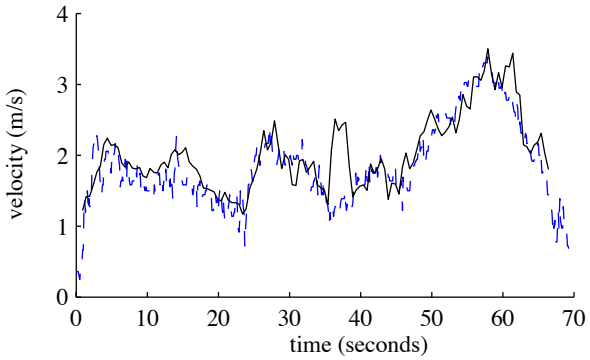

Fig. 6. Balloon horizontal velocity magnitude estimates vs. time for the vision system (solid black line) and GPS (dashed blue line). In this trial, the mean absolute deviation vs. time between the two approaches was 0.24 m/s.

C. Wind field estimation using flight data

To assess the performance of wind field estimation, a flight test was conducted using the Uglo 6 aircraft. The aircraft was flown manually (radio controlled) while telemetry data were logged via the on-board Piccolo SL autopilot system. During the approximately 6.5 minute flight, 9 balloons were launched and tracked with the vision system to estimate the wind field. Figure 7 shows the aircraft flight path, as well as the balloon tracks.

When post-processing the aircraft telemetry data, we observed GPS velocity drops during significant portions of the flight. These drops compromised the aircraft velocity estimates, and as a result the algorithm's ability to estimate wind velocity. As a result, we constrained our analysis to a 80 second window where GPS velocity estimates were *mostly* available.

Figure 8 shows a composite of the wind velocity estimates vs. altitude from portions of 3 balloon tracks that overlapped in time with the flight window. The discrete velocity estimates are shown as red "x" markers. The solid blue line shows a quadratic fit of the data which was used as ground truth for comparison with wind field estimation conducted

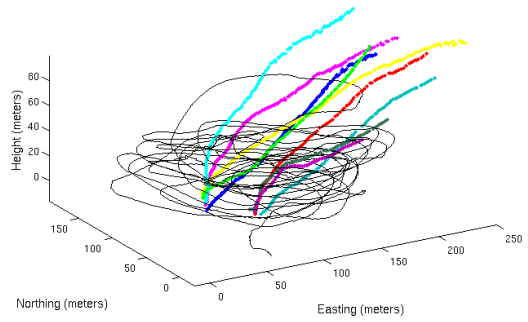

Fig. 7. Aircraft flight path (black solid line) and balloon tracks (dotted color lines) from flight testing. The latter were recovered by the vision tracking system

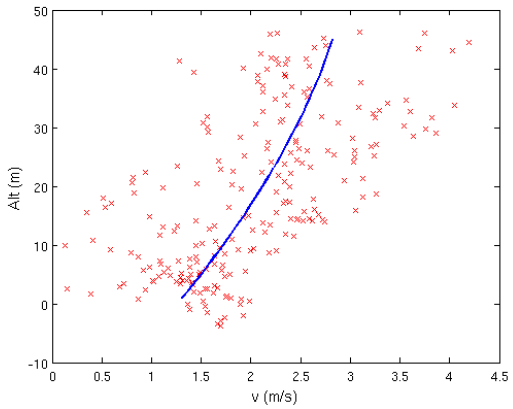

Fig. 8. Wind velocity magnitude vs. altitude as estimated by the vision tracking system. Discrete measurements are shown, as well as a quadratic fit to the data.

using post-processed data from the Piccolo SL autopilot module.

The relevant portion of the flight path is shown in Figure 9. Note that this is not a typical DS trajectory: rather it consists of orbits with slowly changing altitude.

Flight data from the autopilot was post-processed to compute the 3D wind vector and compute an estimate of the wind field using a second order polynomial fit. At the end of the flight window the estimated wind profile was

$$w_f(h) = -2.2631 \times 10^{-4} h^2 + 0.0272h + 1.262 \qquad (19)$$

with h height above ground in meters and w_f is wind speed in m/s. The standard deviations of the terms above are 4.14×10^{-4} for the quadratic term, 0.037 for the linear term and 0.769 for the constant term. The balloon-derived velocity profile is

$$w_b(h) = -3.259 \times 10^{-4} h^2 + 0.04940h + 1.261 \qquad (20)$$

This is well within the range predicted by the post-processed in-flight measurements.

Figure 10 show convergence of the estimated parameters over time. Because the flight path changed altitude slowly

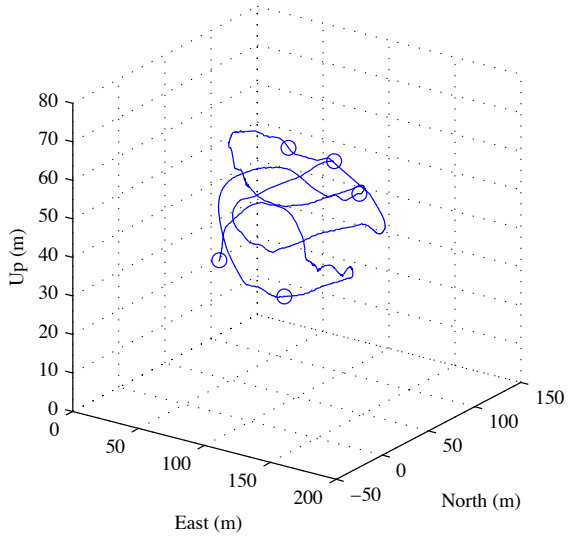

Fig. 9. Portion of flight path used for wind field estimation.

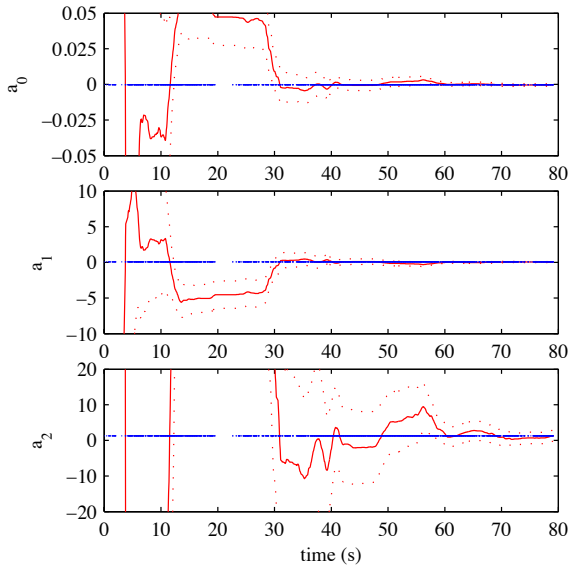

Fig. 10. Wind parameter estimation from flight. Blue lines show parameter values obtained from balloon tracking data, solid red shows the estimated parameter and dotted red shows 2σ bounds.

over time, the temporal convergence of the parameter estimates is quite slow. More dramatic altitude variation would allow faster convergence.

A time history of the estimated wind field is shown in Figure 11. The balloon-obtained second order polynomial curve fit is shown in blue, and shows higher wind speed than obtained from in-flight data. As before, at time zero there is no estimate of wind field. As time progresses one can see the estimated wind field approach ground truth (the balloon data). With a longer flight window, we would expect to see further convergence with the ground truth estimate.

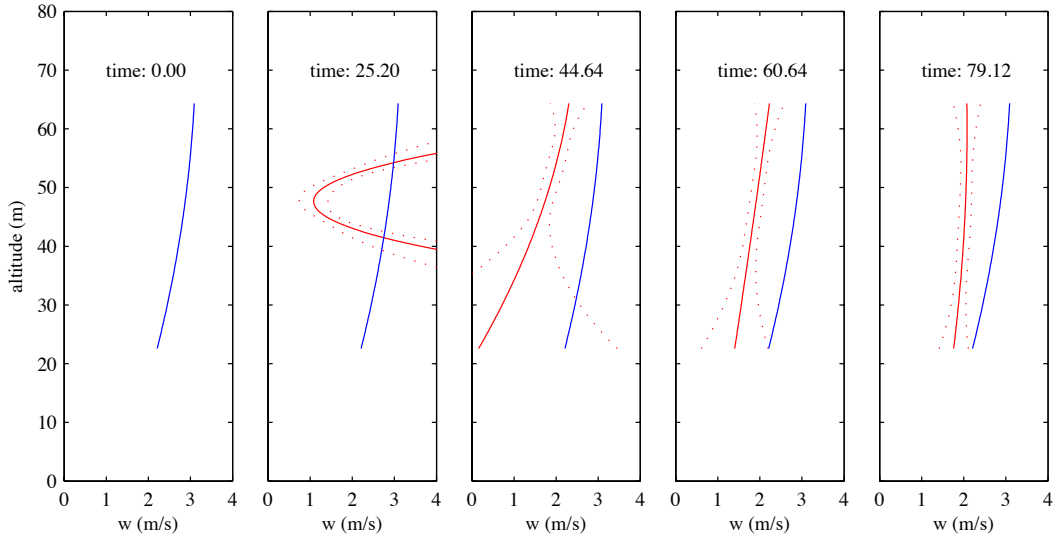

Fig. 11. Time history of wind field estimation from flight data. Blue lines show curve fit of wind velocity obtained from balloon data, solid red shows the estimated field and dotted red shows 2σ uncertainty bounds on the estimated wind field. Times coincide with open blue circles in the flight path of Figure 9.

V. DISCUSSION AND CONCLUSIONS

With an eye to enabling autonomous dynamic soaring on a small unmanned aircraft, this paper has: (a) presented results comparing wind measurements using a vision-based balloon tracking system with wind measurements obtained using an aircraft in flight; (b) described a method based on distributed parameter estimation to compute a map of a wind field; (c) presented results of a Monte Carlo simulation to assess the effectiveness of the parameter estimation.

The wind field is represented using a polynomial approximation. This is well suited to shear layers in the vicinity of the jet stream and the atmospheric boundary layer, however this method may be subject to errors related to both under-approximation and over-approximation. While performance of the wind estimator is good in the linear wind shear case examined here (both the gradient and the wind speed at a reference altitude were well-estimated), some tuning of parameters in the Kalman filter should further improve performance. Future work will focus on using splines to parameterize the wind field. This will obviate potential issues with scaling and will allow parameterization of more complex wind fields than those found near the jet stream or the atmospheric boundary layer (for example, shear layers caused by temperature inversions or flow separation in the lee of a ridge).

With the availability of a wind field estimator that includes estimates of parameter uncertainty, robust dynamic soaring trajectories can be generated without *a priori* knowledge of the wind field (although clearly exploration will be required to generate the wind field estimate).

VI. ACKNOWLEDGMENTS

This research was funded by the National Science Foundation under grants IIS-1065024 and IIS-1065202.

REFERENCES

[1] J. W. S. Rayleigh, "The soaring of birds," *Nature*, vol. 27, pp. 534–535, 1883.
[2] ——, "The sailing flight of the albatross," *Nature*, vol. 40, p. 34, 1889.
[3] F. W. Lanchester, *Aerodonetics*. D. Van Nostrand Company, 1909.
[4] E. P. Warner, "Soaring without rising currents," National Adivsory Committee for Aeronautics," Technical Memorandum, 1923.
[5] W. B. Klemperer, "A review of the theory of dynamic soaring," in *Proceedings of the 7th OSTIV Congress*, Poland, June 1958.
[6] F. Hendricks, "Dynamic soaring," Ph.D. dissertation, University of California, Los Angeles, Los Angeles, California USA, 1972.
[7] M. B. E. Boslough, "Autonomous dynamic soaring platform for distributed mobile sensor arrays," Sandia National Laboratories, Sandia National Laboratories, Tech. Rep. SAND2002-1896, 2002.
[8] G. Sachs and O. da Costa, "Dynamic soaring in altitude region below jet streams," in *AIAA Guidance, Navigation and Control Conference*, no. AIAA Paper 2006-6602, Keystone, Colorado, August 21-24 2006.
[9] T. Kiceniuk, "A variometer for dynamic soaring," *Technical Soaring*, vol. 25, no. 4, pp. 231–234, October 2001.
[10] R. J. Gordon, "Optimal dynamic soaring for full size sailplanes," Master's thesis, Air Force Institute of Technology, Wright-Patterson Air Force Base, September 2006.
[11] Y. J. Zhao, "Optimal patterns of glider dynamic soaring," *Optimal Control Applications and Methods*, vol. 25, no. 2, pp. 67–89, 2004.
[12] N. R. J. Lawrance and S. Sukkarieh, "Simultaneous exploration and exploitation of a wind field for a small gliding uav," in *AIAA Guidance, Navigation and Control Conference*, AIAA Paper 2010-8032. American Institute of Aeronautics and Astronautics, 2010.
[13] J. W. Langelaan, N. Alley, and J. Neidhoefer, "Wind field estimation for small unmanned aerial vehicles," *AIAA Journal of Guidance, Control and Dynamics*, vol. 34, no. 4, pp. 1016–1030, 2011.
[14] F. M. White, *Viscous Fluid Flow*, 3rd ed. New York, NY: McGraw-Hill, 2006.
[15] J. Grenestedt and J. Spletzer, "Towards Perpetual Flight of a Gliding Unmanned Aerial Vehicle in the Jet Stream," in *Proc. IEEE Conf. on Decision and Control*, Atlanta, GA, Dec 2010.
[16] R. Hartley, "In defense of the eight-point algorithm," *IEEE Transactions on Pattern Analysis and Machine Intelligence*, vol. 19, no. 6, pp. 580–593, June 1997.
[17] *Instruction Manual for the Micro GPS Expander V4*, 1st ed., Eagle Tree Systems, 2010.